NeuroImage 243 (2021) 118489

Contents lists available at ScienceDirect

NeuroImage

journal homepage: www.elsevier.com/locate/neuroimage

Microstructural properties within the amygdala and affiliated white matter tracts across adolescence

Anisa Azad[a], Ryan P. Cabeen[b], Farshid Sepehrband[b], Robert Kim[a], Claire E. Campbell[a], Kirsten Lynch[b], J. Michael Tyszka[d], Megan M. Herting[a,c,*]

[a] Department of Population and Public Health Science, Keck School of Medicine, University of Southern California, 2001 N Soto, Los Angeles, CA 90032, USA
[b] Laboratory of Neuro Imaging, USC Stevens Neuroimaging and Informatics Institute, Keck School of Medicine, University of Southern California, Los Angeles, CA, USA
[c] Department of Pediatrics, Keck School of Medicine, University of Southern California, Los Angeles, CA, USA
[d] Division of Humanities and Social Sciences, California Institute of Technology, Pasadena, CA, USA

ARTICLE INFO

Keywords:
Neurodevelopment
Amygdala
Adolescence
Sex differences
Diffusion
Tractography

ABSTRACT

The amygdala is a heterogenous set of nuclei with widespread cortical connections that continues to develop postnatally with vital implications for emotional regulation. Using high-resolution anatomical and multi-shell diffusion MRI in conjunction with novel amygdala segmentation, cutting-edge tractography, and Neurite Orientation Dispersion and Density (NODDI) methods, the goal of the current study was to characterize age associations with microstructural properties of amygdala subnuclei and amygdala-related white matter connections across adolescence ($N = 61$, 26 males; ages of 8–22 years). We found age-related increases in the Neurite Density Index (NDI) in the lateral nucleus (LA), dorsal and intermediate divisions of the basolateral nucleus (BLDI), and ventral division of the basolateral nucleus and paralaminar nucleus (BLVPL). Additionally, there were age-related increases in the NDI of the anterior commissure, ventral amygdalofugal pathway, cingulum, and uncinate fasciculus, with the strongest age associations in the frontal and temporal regions of these white matter tracts. This is the first study to utilize NODDI to show neurite density of basolateral amygdala subnuclei to relate to age across adolescence. Moreover, age-related differences were also notable in white matter microstructural properties along the anterior commissure and ventral amydalofugal tracts, suggesting increased bilateral amygdalae to diencephalon structural connectivity. As these basolateral regions and the ventral amygdalofugal pathways have been involved in associative emotional conditioning, future research is needed to determine if age-related and/or individual differences in the development of these microstructural properties link to socio-emotional functioning and/or risk for psychopathology.

1. Introduction

The amygdala plays an important role in emotion processing (Phelps and LeDoux, 2005) and the functions of the amygdala are modulated through its widespread connections to cortical and subcortical regions through several major white matter tracts (Abivardi and Bach, 2017). Structurally, the amygdala continues to develop across adolescence (Giedd et al., 1996; Herting et al., 2018) as does the prefrontal cortex (Sowell et al., 2002; Tamnes et al., 2017), with the dynamic interactions between the two structures contributing to the increasing ability for children and adolescents to regulate their emotions (Kim et al., 2011). While the field has made great strides in understanding child and adolescent development of total amygdala volumes as well as examining amygdala-related white matter connectivity using diffusion tensor imaging (DTI) (Ho et al., 2019; Rus et al., 2017), more recent advancements in anatomical and diffusion neuroimaging have improved our ability to further elucidate age-related differences in both the neurite density of subnuclei within the amygdala as well as axonal properties of white matter projections of the amygdala in children and adolescents. Such methods include *in vivo* derived amygdala subnuclei atlases (Tyszka and Pauli, 2016) and Neurite Orientation Dispersion and Density Imaging (NODDI) (Zhang et al., 2012). The goal of the current study was to utilize a multi-modal neuroimaging approach to elucidate age-related differences in microstructural properties of amygdala subnuclei and amygdala white matter connections in children and adolescents. By understanding age related variation in gray and white matter microstructure of the amygdala and its projections, these findings may help us to further understand amygdala development as well as possi-

* Corresponding author at: Department of Population and Public Health Science, Keck School of Medicine, University of Southern California, 2001 N Soto, Los Angeles, CA 90032, USA.
E-mail address: herting@usc.edu (M.M. Herting).

https://doi.org/10.1016/j.neuroimage.2021.118489.
Received 27 April 2021; Received in revised form 16 July 2021; Accepted 19 August 2021
Available online 24 August 2021.

ble amygdala related abnormalities that may confer risk for affective disorders that begin to emerge across adolescence (Kessler et al., 2005).

Although traditionally examined as a single structure in human magnetic resonance imaging (MRI), the amygdala is in fact heterogeneous, and consists of various functionally and anatomically distinct subnuclei that may have unique patterns of development. Specifically, a recent post-mortem histological study that included brain samples from individuals ranging from the ages of 2 to 48 years found significant increases in amygdala neuron number with age, with the largest effect seen in the paralaminar and basal nucleus (Avino et al., 2018). The human paralaminar region was also found to contain excitatory neurons that remain immature across postnatal life, providing a possible substrate for continued neuroplasticity in the amygdala (Sorrells et al., 2019). As such, a recent cross-sectional structural MRI study by our team utilized a novel *in vivo* derived amygdala subnuclei atlas (Tyszka and Pauli, 2016) to examine age-related differences in amygdala subnuclei volumes across adolescence ($N = 408$, mean age = 14.12 years) (Campbell et al., 2021). We found that the relative volume fraction of a number of specific nuclei within the amygdala, including the lateral, basolateral ventral and paralaminar subdivision (BLVPL), and central nucleus, increased with age in males. Yet, questions remain as to whether other *in vivo* microstructural changes occur within the human amygdala across adolescence. To this end, Neurite Orientation Dispersion and Density Imaging (NODDI) is a multi-compartment biophysical model that decomposes signals from three tissues compartments (neurites, extra-neurites and cerebrospinal fluid) (Fukutomi et al., 2019) and can be used to estimate microstructural tissue properties *in vivo*, including cellular features such as neurite density and orientation dispersion (Zhang et al., 2012). Moreover, NODDI parameters are in good agreement with histological measures (Grussu et al., 2015; Sepehrband et al., 2015), suggesting that NODDI is an appropriate model to understand the biological properties of the microstructural changes *in vivo*. To date, one small study ($N = 27$) has reported increased neurite density of the total amygdala using NODDI in 8 to 13 year-olds (Mah et al., 2017). However, no study has utilized NODDI to examine neurodevelopmental changes in microstructure within specific amygdala subnuclei across adolescence.

Beyond developmental patterns within each subnuclei themselves, the amygdala has extensive connections with the cortex and other subcortical structures. Primary efferent pathways of the amygdala include the ventral amygdalofugal pathway, stria terminalis, and anterior commissure (Noback et al., 2005). The ventral amygdalofugal pathway connects the basolateral and central nuclei of the amygdala to the thalamus, bed nucleus of the stria terminalis (BNST), nucleus accumbens, and hypothalamus (Lovblad et al., 2014; Pascalau et al., 2018; Shah et al., 2012; Weller and Smith, 1982). The stria terminalis primarily carries fibers from the centromedial portion of the amygdala to the hypothalamus and BNST (Lebow and Chen, 2016; Lovblad et al., 2014; Weller and Smith, 1982), whereas bilateral connections between the amygdala and temporal pole are projected to one another via the temporal branch of the anterior commissure (Catani and Thiebaut de Schotten, 2008). A handful of prior diffusion weighted imaging studies have utilized diffusion tensor imaging (DTI) or other techniques such as probabilistic tractography and *Q*-space diffeomorphic reconstruction to understand structural connectivity changes of the amygdala during development (Jalbrzikowski et al., 2017; Saygin et al., 2015), which may not fully capture the underlying biological changes in white matter. Specifically, while these techniques may be useful for fiber tracking and understanding white matter integrity, these parameters lack specificity about the biological properties underlying the microstructural changes (Edwards et al., 2017). For example, DTI provides us with values of fractional anisotropy (FA), however FA is affected by both neurite density and orientation dispersion. NODDI on the other hand allows us to interpret whether microstructural changes observed in FA are due to the volume of neurites or the geometry of neurite orientation (Fukutomi et al., 2019). Only a few studies have utilized NODDI to examine age-related cellular architecture in various white matter tracts during childhood and adolescence (7–13 years) (Chang et al., 2015; Genc et al., 2017; Mah et al., 2017); however, to our knowledge no study has utilized tractography to delineate the ventral amygdalofugal pathway in order to thoroughly characterize NODDI based microstructural patterns in all three of the primary amygdala-specific pathways (i.e. ventral amygdalofugal pathway, stria terminalis, and anterior commissure).

In this study, our goal was to utilize NODDI to elucidate age-related differences in microstructural properties within amygdala subnuclei as well as amygdala white matter efferents in children and adolescents. While prior segmentation methods utilized *ex vivo* MRI and histological data to parcellate the amygdala based on post-mortem brains from older adults with an average age in the mid-60s (Amunts et al., 2005; Saygin et al., 2015), new methods, such as the high-resolution probabilistic atlas (CIT168), allows for the segmentation of amygdala subnuclei *in vivo* in both adults (Pauli et al., 2018; Tyszka and Pauli, 2016) and pediatric populations (Campbell et al., 2021; Herting et al., 2020). We utilized each subject's T1-weighted and T2-weighted images and the CIT168 atlas to segment the amygdala into 9 distinct bilateral subnuclei (Pauli et al., 2018; Tyszka and Pauli, 2016) and developed a multi-fiber tractography protocol to delineate the three amygdala white matter tracts of interest, including the anterior commissure, stria terminalis, and ventral amygdalofugal pathway. Beyond the primary efferents of the amygdala, for completeness we also examined microstructure in three additional white matter tracts that have been identified to be involved with carrying information between the medial temporal lobe structures, including the amygdala and hippocampus, to the prefrontal cortex and other subcortical structures. These include the cingulum bundle, carrying fibers from the medial temporal lobe to the cingulate cortex (Heilbronner and Haber, 2014; Pascalau et al., 2018); the fornix, which innervates the hippocampus, nucleus accumbens, and mammillary bodies (Pascalau et al., 2018); and the uncinate fasciculus that connects the anterior temporal lobe to the orbitofrontal cortex (Pascalau et al., 2018; Von Der Heide et al., 2013). Furthermore, to be comprehensive we also examined age associations with common DTI outcomes. Given that NODDI parameters have been found to be more sensitive to the effects of age than DTI (Genc et al., 2017), we expected age associations would be more prominent for NODDI estimates of amygdala gray matter and white matter microstructure. Given previous studies that have found sex differences as well as physical characteristics to relate to total amygdala volumes (Giedd et al., 1996; Orsi et al., 2011) and white matter microstructure (Geeraert et al., 2019; Herting et al., 2018; Kullmann et al., 2015), we also explored if microstructural properties differed between males and females. Given previous postmortem findings that developmental trajectories of neuron numbers within amygdala subnuclei change with age (Avino et al., 2018), we expected increased neurite density in basolateral subnuclei across adolescence. Moreover, given known increases in myelination throughout childhood and adolescence (Benes et al., 1994; Yakovlev and Lecours, 1967) and generation of new oligodendrocytes throughout development and even into adulthood, we hypothesized to also observe age-related associations with NODDI metrics across all six white matter tracts of interest. We also expected that NODDI parameters may vary between amygdala subnuclei given histological data on the human amygdala indicate that there are compositional differences between subnuclei (neuron number, soma volume, neuron density) (Chareyron et al., 2011; Schumann and Amaral, 2005).

2. Materials and methods

2.1. Participants

This study analyzed data from 63 typically developing individuals (35 female, 28 male) between the ages of 8 and 22 years old at the time of their visit. Data for this study was collected from two separate study samples: one from children and adolescents in the age range of 8 to 18 years and another from young adults in the age range of 19 to 23 years (**Supplemental Fig. 1**). Both studies underwent an identi-

cal neuroimaging protocol acquired on the same 3 Tesla MRI scanner at the University of Southern California's Center for Image Acquisition. Both research projects were approved by the local institutional review board and informed consent/assent was obtained from parents and children prior to data collection. All subjects were screened for any significant neurological conditions (e.g. epilepsy, traumatic head injury) and psychiatric/developmental disorders (e.g. autism, attention deficit hyperactive disorder, schizophrenia, self-harm tendencies), which barred participation. Subjects were also screened for any factors that would prevent effective and safe use of MRI, such as irremovable ferrous materials (e.g. braces), uncorrectable vision impairments (e.g. blind spots, color-blindness), need for hearing aids, or claustrophobia. Health-related exclusionary criteria for all participants included prenatal drug or alcohol exposure, premature birth, serious medical illness, eating disorders, or psychotropic medication. In order to more fully characterize our sample, the NIH Toolbox demographics form was completed from the child's parents or the young adult participants, including handedness, race, ethnicity, and maternal education (Gershon et al., 2013). For all participants, height and weight were measured and a SAS program based on the 2000 CDC Growth Charts (ages 0 to 20 years) was used to calculate body mass index (BMI) as well as weight-for-height z-scores (BMI z-score) based on the individual's age and biological sex (Kuczmarski et al., 2002; CDC SAS Program, 2019). Pubertal development was assessed in children (<18 years-old) by a physician using Tanner staging criteria (Tanner, 1981). IQ was assessed in all participants using the Wechsler Abbreviated Scale of Intelligence (WASI-II) (Wechsler, 2011).

2.2. Magnetic resonance imaging acquisition and quality control

All images were collected on a single Siemens Magnetom Prisma 3 Tesla MRI scanner using a 32-channel head coil at the University of Southern California's Center for Image Acquisition. 3D T1-weighted (T1w) and T2-weighted (T2w) structural images were acquired using sagittal whole brain MPRAGE sequences (T1w: TR = 2400 ms, TE = 2.22 ms, flip angle = 8°, BW = 220 Hz/Px, FoV = 256 mm, 208 slices, and 0.8 mm isotropic voxels, with a GRAPPA phase-encoding acceleration factor of 2; T2w: TR = 3200 ms, TE = 563 ms, BW = 744 Hz/pixel, FoV = 256 mm, 208 slices, 0.8 mm isotropic voxels, and 3.52 ms echo spacing, with a GRAPPA phase-encoding acceleration factor of 2). Anterior-posterior and posterior-anterior spin echo field maps were also obtained (TR = 8000 ms, TE = 66.0 ms, flip angle = 90°, BW = 2290 Hz/pixel, FoV = 208 mm, 72 slices, and 2.0 mm isotropic voxels).

Multi-shell diffusion-weighted MRI with *b*-values of 0, 1000 and 2500 s/mm^2 were acquired to enable microstructural modeling (Sepehrband et al., 2017; Zhang et al., 2012). A 32-channel head array (Nova Medical Inc, Wilmington MA) was used for radiofrequency signal reception with body coil radiofrequency transmission. An optimally distributed multi-shell diffusion-encoding sampling scheme, consisting of 100 directions (33 and 67 directions for b-values of 1000 and 2500 s/mm^2, respectively) was designed using the *q-space sampling* web application (Caruyer et al., 2013). Diffusion-encoding gradients were acquired in both anterior-posterior (AP) and posterior-anterior (PA) phase encoding directions to allow EPI distortion correction. Eleven interleaved unweighted diffusion (b0) gradients were acquired for each phase encoding direction. Total diffusion MRI scan time was 15 min. and 22*s* (total of 222 images). Other diffusion MRI sequence parameters: 81 slices, 2.0 mm isotropic voxels, matrix size = 116 × 116, field-of-view = 232 × 232 mm, fixed TE of 72 ms and a TR of 4000 ms, and effective echo spacing of 0.55 ms, phase partial Fourier 6/8, iPAT acceleration factor 3 with a monopolar diffusion-encoding sequence.

Motion assessments and image exclusion

All scans were reviewed by a radiologist for incidental findings of abnormalities. All raw structural images were visually inspected to assess motion and were rated a Pass, Check, or Fail (Backhausen et al., 2016). Qualitative and quantitative methods were utilized to assess the effects of motion on the quality of the DWI images. First, all raw DWI images were visually examined for artifacts due to motion, including signal dropout in the axial plane in each of the 222 gradient volumes. Next, an open-source, automated quality control script was used to calculate motion using the mean relative volume-to-volume translation and rotation of the 11 interspersed b0 images (Roalf et al., 2016). Roalf (2016) sets an exclusion threshold on motion greater than 1.89 mm, thus any subject that exceeded a value of 1.89 mm for motion was excluded from further analyzes.

2.3. MRI preprocessing

We designed an analytic workflow for quantitative analysis of tissue microstructure and white matter connectivity using our collected structural and diffusion MRI data. We used a template-based approach to obtain geometric models of white matter fiber bundles, and we further characterized tissue properties of the fiber bundles and amygdala subfields.

Structural preprocessing

All structural images underwent processing and whole brain segmentation using Freesurfer v6.0 (http://surfer.nmr.mgh.harvard.edu) (Fischl et al., 2002; Reuter et al., 2012). All postprocessed images were visually inspected by a trained operator to assess the accuracy of segmentation for each participant. No manual intervention was performed.

DWI preprocessing

Standard DWI preprocessing was performed using a combination of the FSL Diffusion Toolbox (Jenkinson et al., 2012), DTI-TK (http://dti-tk.sourceforge.net/pmwiki/pmwiki.php) (Zhang et al., 2006), and the Quantitative Imaging Toolkit (QIT) (http://cabeen.io/qitwiki) (Cabeen et al., 2018). First, AP and PA acquisitions were intensity normalized and images underwent EPI image distortion correction using FSL TOPUP. Images were then corrected for eddy current effects, magnetic field inhomogeneities, and head motion using FSL EDDY (Jenkinson, 2003). Brain masks were extracted from the average baseline diffusion scan using BET (Smith, 2002). To assess tissue microstructure, we performed Neurite Orientation Dispersion and Density Imaging (NODDI) (Zhang et al., 2012) using the grid-search algorithm in the VolumeNoddiFit module of QIT. For tractography analysis, we also estimated ball-and-stick models using FSL BEDPOSTX (Behrens et al., 2007) using the multi-shell model and up to three fiber compartments per voxel. We then performed spatial normalization of each subject's diffusion data to the IIT template (Zhang et al., 2011) using the deformable tensor-based registration algorithm in DTI-TK; the resulting deformations were retained for subsequent analysis. For completeness, we also estimated diffusion tensor indices using FSL DTIFIT, including fractional anisotropy (FA), mean diffusivity (MD), axial diffusivity (AD), and radial diffusivity (RD) (Assaf and Pasternak, 2008).

Amygdala segmentation and subnuclei microstructural analyzes

We used a multi-modal approach that combines T1w, T2w MRI and DWI data to analyze microstructure imaging parameters in amygdala subnuclei. Details of the CIT168 *in vivo* amygdala probabilistic atlas construction, validation, estimates of individual differences, and comparison with previous atlases have been previously published (Pauli et al., 2018; Tyszka and Pauli, 2016). Amygdala subnuclei were estimated at the individual level for each child and adolescent as previously published (Herting et al., 2020). Briefly, each participant's T1w and T2w image were rigid-body AC-PC aligned (Tyszka and Pauli, 2016) and then registered to the CIT168 atlas using a bivariate B-spline analog of the symmetric normalization diffeomorphic registration algorithm (B-Spline SyN) from ANTs (Avants et al., 2007; Tustison and Avants, 2013). Each subject's T1w and T2w signal intensities for both hemispheres of the amygdala are plotted in **Supplemental Fig. 2**. Probabilistic labels in the CIT168 atlas space were mapped to individual spaces using an inverse diffeomorphism, allowing probabilistic segmentation of each participant's left and right entire amygdala and the following 9 bilateral regions of interest (ROI): lateral nucleus (LA); dorsal and intermediate

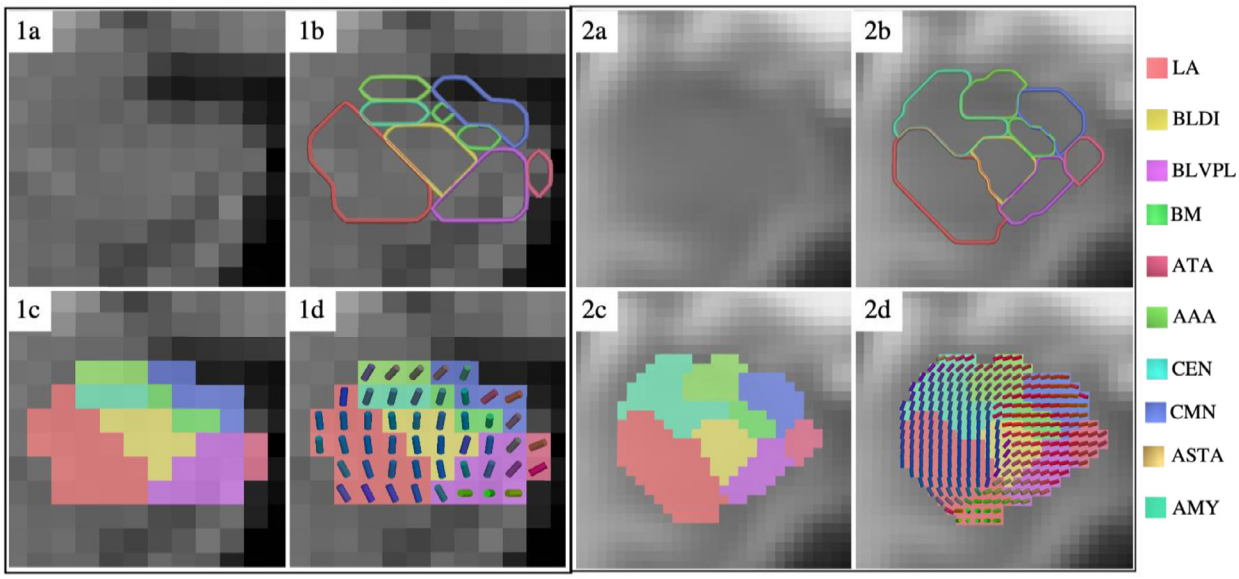

Fig. 1. Enlargement of the rostral-caudal view of the right amygdala for an individual at 2mm^3 resolution (1) and the average at 1mm^3 resolution (2) on the NDI parameter map; (a) only the NDI parameter map; (b) outline of the amygdala subregions on NDI parameter map; (c) overlay of amygdala subregions on NDI parameter map; (d) neurite vectors for the NDI parameter map overlayed on top of the overlay of amygdala subregions. 3D cylinder glyphs are overlaid on 1d and 2d to show the primary axis of the NODDI intra-cellular tissue compartment, with coloring in a typical scheme where the direction vector is normalized to provide RGB values that correspond to XYZ vector coordinates.

divisions of the basolateral nucleus (BLDI); ventral division of the basolateral nucleus and paralaminar nucleus (BLVPL); basomedial nucleus (BM); central nucleus (CEN); cortical and medial nuclei (CMN); amygdala transition areas (ATA); amygdalostriatal transition area (ASTA); and anterior amygdala area (AAA) (**Supplemental Fig. 3**). Volumes of the CIT168 amygdala subnuclei in our study sample are plotted in **Supplemental Fig. 4**. We also created an average T1w brain and T2w of our study sample by aligning and averaging all the T1w and T2w images (n = 61) from our dataset in order to provide a comparison to the young adult CIT168 atlas (**Supplemental Figs. 5 and 6**). Given that the registration cost function relies on regional signal contrast both within and in the immediate neighborhood of the amygdala, Tyszka and Pauli (2016) examine in their original paper how individual T1/T2-weighted contrast to noise (CNR) may impact registration accuracy of the CIT168 atlas in order to generate meaningful registration of amygdala subregions in the presence of noise. They determined a CNR greater than 1.0 within the amygdala allows for a robust volume estimation of the ground truth volumes of a subregion when using the ANTs SyN algorithms with appropriate regional cost-functions. Thus, the intensity contrast within each hemisphere of the amygdala was estimated from the interquartile range of intensities within the entire amygdala from each subject's T1-weighted image. The standard deviation (SD) of the noise was estimated from the residual signal obtained from the subtracted T1-weighted atlas template image from each subject's T1w image. The interquartile range (IQR) was then divided by the mean residual noise SD to generate the CNR for each individual. The average CNR for the current study was 1.11 for the left amygdala and 1.14 for the right amygdala. Importantly, in order to determine if age-related differences in CNR may impact the amygdala segmentation capabilities across our sample, we also examined if the CNR or the signal and noise components (i.e. signal IQR and SD of the noise) that were used to derive the CNR were associated with age. There were no significant associations between T1- or T2-weighted CNR within the amygdala, signal IQR, or SD of noise (range of correlations coefficients were -0.03 to -0.23, with all p-values > 0.05).

To examine microstructural properties within each amygdala subnuclei, each subject's structural image was registered to the DWI image using ANTs' nonlinear registration algorithm, symmetric normalization (SyN), where the "moving" image was the first $b0$ baseline volume from the DWI images and the "fixed" image was the T1w rigid-body AC-PC aligned image. Next, to align the probability estimates of the amygdalae to the subject diffusion data, the inverse warp was applied to the left and right probability estimates using ANTs linear interpolation. Based on the probability to belong to a given subnuclei, a Winner-Takes-All approach was used to assign each voxel within the amygdala to 1 of 9 subnuclei. Average microstructure parameters were then calculated for each subnuclei. An example of an amygdala subnuclei mask overlayed on an NDI map is shown in **Fig. 1**.

Diffusion white matter tractography

We designed a multi-fiber tractography workflow for automated modeling of white matter fiber bundles associated with the amygdala. We used a template-based approach to delineate population-averaged fiber bundle models that were then used to guide the segmentation of analogous bundles in individual subject datasets (Cabeen and Toga, 2020). Given our *a priori* interest in understanding amygdala white matter connectivity, our analysis included six tracts that were manually delineated *a priori* reference bundles using anatomical guidelines. We first generated an averaged multi-fiber dataset in IIT template space using 80 subjects from the Human Connectome Project and a kernel regression framework for interpolating and averaging ball-and-sticks models (Cabeen et al., 2016), which was implemented using the VolumeFibersTransform and VolumeFibersFuse modules in QIT. Next, regions of interest (ROI) were drawn on the multi-fiber IIT template using the specific guidelines for each bundle described in detail in Supplemental Material. Multi-fiber streamline tractography was then performed using the averaged reference dataset to create a reference bundle mask, and tract orientation maps were computed using the CurvesOrientationMap module in QIT, which finds the average bundle orientation in each template voxel (Wasserthal et al., 2018). We used bundle-specific tractography seed points, which were found by sampling 10,000 points equally distributed across the reference bundle mask using the MaskSampleVects module in QIT. Bundle reference masks and their associated seeds and orientation maps were then deformed to each subject's native space using the DTI-TK deformation field, and these were used as anatomical priors for performing reinforcement tractography (Cabeen and Toga, 2020) using the VolumeModelTrackStreamline mod-

ule in QIT. The reinforcement tractography algorithm segments bundle-specific fiber orientations based on the reference tract orientation map then performs tractography with deterministic streamline integration. Our tracking parameters included a minimum fiber volume fraction of 0.075, a maximum turning angle of 75°, and trilinear interpolation during streamline integration. The resulting tract models were visualized at the single-subject level to ensure tract accuracy. Our criteria for delineating each of the six bundles are described in detail in Supplemental Material.

Average and along-tract microstructural white matter analyzes

For each subject, each of the 6 bundles was then quantitatively summarized with respect to volume, length, and average microstructure parameters for NODDI (NDI, ODI) as well as DTI (FA, MD, RD, AD). In addition to averaging diffusion parameters across the entire tract, we also performed along-tract analyzes to determine if associations with age were heterogeneous at various points along each white matter bundle. In order to perform along-tract analyzes, each tract was subdivided into equidistant points using an automated approach based on Colby et al. (2012) and implemented with the CurvesSegmentAlong module in QIT. A prototypical curve was first established in template space by identifying the "centroid" curve with the minimum Hausdorff distance to the other streamlines. The prototypical curve was then resampled with vertices every 5mm in order to represent discretized regions along the length of the bundle and was registered to subject native space using DTI-TK. In order to create correspondence among cross-sectional points for a given tract, streamline vertices were interpolated to best match the prototypical curve for each subject's tract. Diffusion parameters were then sampled and averaged over each group of shared vertex labels that match the reference prototypical curve and the subsequent along-tract parameter maps were used for statistical analysis.

2.4. Statistical analyzes

All of the analyses were conducted in R (version 3.6.1) and lme4 package (version 1.1-21) (Bates et al., 2015). Although there was not a significance sex difference in motion ($p = 0.41$), we also assessed if motion was related to age, and if these associations were different by sex using linear regressions. Motion was found to relate to age ($p \leq 0.01$) and this association was driven by males (age-by-sex interaction: $p \leq 0.05$). Therefore, we included motion as a covariate in all analyses. Next, separate linear multi-level models were used to assess microstructure properties in relation to age, sex, and their interaction for the whole amygdala and each of its 9 subnuclei, while covarying for BMI z-score (BMIz), maternal education, race, hemisphere, motion, and the volume of each region, with the random effect of subject. Maternal education was categorized in 3 groups: (1) high school graduate and lower, (2) some college and above, or (3) not provided. Race was categorized into 4 groups: (1) White, (2) Black or African American, (3) Asian, American Indian or Alaskan Native, Native Hawaiian or other Pacific Islanders, Other, or more than one race, and (4) not provided. Separate multi-level models were used to assess microstructure of each tract in relation to age, sex, and their interaction, while covarying for BMIz, hemisphere, the number of streamlines within the tract, and motion. As the anterior commissure is not a bilateral tract, an identical linear regression was used without the repeated measure of hemisphere included in the model. Standardized estimates were calculated for any model where a significant effect was found using the sjPlot tab_model function in R which is performed by completely refitting the model on the standardized data. Lastly, following the identification of significant age associations for a given tract, follow-up analyses were done using linear multi-level models to examine the microstructural properties along each tract in relation to age and sex, while covarying for BMIz, hemisphere, motion, and the number of streamlines with the tract, with the random effect of subject. An ANOVA was then performed for each model to assess the significance of the interaction of age by diffusion parameter along the tract. All p-values were corrected for multiple comparisons using false discovery rate correction from the p.adjust function in the R package 'stats' (v3.6.2). FDR corrections were applied to models assessing NODDI and DTI parameters within the amygdala and its 9 subnuclei (20 models for NODDI parameters; 40 models for DTI parameters), as well as the 5 bilateral (i.e. ventral amygdalofugal pathway, cingulum, stria terminalis, fornix, and uncinate fasciculus) and 1 bihemispheric (i.e. anterior commissure) amygdala-related tract analyses (12 models for NODDI parameters; 24 models for DTI parameters). For results passing FDR adjustment ($p < 0.05$), we report effect sizes using partial R-squared (R^2) or omega squared (ω^2) for predictors from our multiple regression and multi-level models, respectively.

3. Results

3.1. Study sample characteristics

One subject was removed from further analyses due to an incidental finding of the brain and another was removed for excessive motion. Our final study sample included 61 children and adolescents, 26 males and 35 females (16.92 ± 4.64 years). For the fornix and stria terminalis, only 60 subjects were examined as one subject did not pass visual quality control of the two tracts. Complete demographics of the study sample for N = 61 are shown in **Table 1**.

3.2. Microstructural properties of the amygdala

The range and mean of the NODDI and DTI measures within the amygdala and its subnuclei are shown in **Supplemental Table 1** and NDI and ODI maps are shown in **Supplemental Fig. 7**. For the whole amygdala, there was no significant age association for NDI or ODI. Microstructural results by amygdala subnuclei can be found in **Table 2**. A significant positive association was seen between NDI and age in the subnuclei of the LA (ω^2=0.29, $p \leq 0.01$), BLDI ($\omega^2 = 0.29$, $p \leq 0.01$), and BLVPL ($\omega^2 = 0.21$, $p \leq 0.05$) **(Fig. 2a,b).** Based on the standardized beta coefficients for age effects in Table 2, increasing age by 4.6 years (standard deviation of age) results in a .54, .55, and .43 change in NDI within the LA, BLDI, and BLVPL, respectively. There was no association between ODI and age. Additionally, neither NDI nor ODI were associated with sex or an age-by-sex interaction. After FDR correction, none of the DTI output measures were associated with age, sex, or an age-by-sex interaction in any of the subnuclei (**Supplemental Tables 2 and 3**).

3.3. Microstructural properties of amygdala white matter connectivity

The range and mean of the NODDI and DTI measures of the white matter tracts are shown in **Supplemental Table 4**. White matter tracts with respect to the amygdala are presented in **Supplemental Fig. 8s.** Four of the six identified white matter connections also showed positive NDI associations with age: ventral amygdalofugal pathway (ω^2= 0.23, $p \leq 0.01$), cingulum (ω^2= 0.36, $p \leq 0.001$), uncinate fasciculus (ω^2= 0.29, $p \leq 0.005$), and anterior commissure (partial $R^2 = 0.32$, $p \leq 0.01$) **(Fig. 3a**, **Table 3**). Standardized beta coefficients in Table 3 show that by increasing age by 4.6 years results in a .52, .60, .43, and .51 change in NDI in the ventral amygdalofugal pathway, cingulum, uncinate fasciculus, and anterior commissure, respectively. After FDR correction, a significant positive association between age and ODI was found in the anterior commissure (partial $R^2 = 0.11$, $p < 0.05$) **(Fig. 3b).** An increase by 4.6 years resulted in an increase of .29 in ODI in the anterior commissure. There were no other associations between NODDI output measures and age, sex, or age-by-sex interaction (**Table 3**). No associations between DTI output measures and age, sex, or age-by-sex were found (**Supplemental Tables 5 and 6**).

3.4. Along-tract microstructural properties

In order to determine if the age effects were heterogenous in tracts identified as significant, we examined age associations with NDI and

Table 1
Study sample.

	All (N = 61)	Males (N = 26)	Females (N = 35)	Group difference
Age, yrs	16.92 ± 4.64	16.75 ± 4.99	17.05 ± 4.43	p = 0.81
Right Handed, n	53 (86%)	23 (88%)	30 (86%)	$\chi^2(1)$ =5.818ε−32; p = 1.00
Hispanic, n	31 (51%)	11 (42%)	20 (57%)	$\chi^2(2)$ =1.31; p = 0.52
Race, n White				$\chi^2(8)$ =9.59; p = 0.29
Black or African American	31	12	19	
Asian	5	4	1	
American Indian/Alaskan Native	2	0	2	
Native Hawaiian/Pacific	1	1	0	
Islander	1	0	1	
More than one race	3	1	2	
Other	12	5	7	
Not Provided	6	3	3	
Maternal Education, n				$\chi^2(12)$ =12.21; p = 0.43
< High School	6	4	2	
High School Degree	7	2	5	
Some college	15	3	12	
College	17	6	11	
Professional Degree	10	7	3	
Not provided	6	4	2	
IQ[a]	103.36 ± 13.50	102.46 ± 14.53	104.03 ± 12.85	p = 0.66
BMI z-score[b]	0.94 ± 0.84	1.13 ± 0.80	0.80 ± 0.86	p = 0.13
Motion[c]	0.69 ± 0.30	0.73 ± 0.32	0.67 ± 0.30	p = 0.41

Mean ± Standard Deviation unless otherwise noted.
[a] General Intelligence measured by the Wechsler Abbreviated Scale of Intelligence (WASI-II)
[b] BMI z-score calculated using the SAS program based on the 2000 CDC Growth Charts
[c] Motion calculated using an automated QC script measuring mean volume-to-volume translation

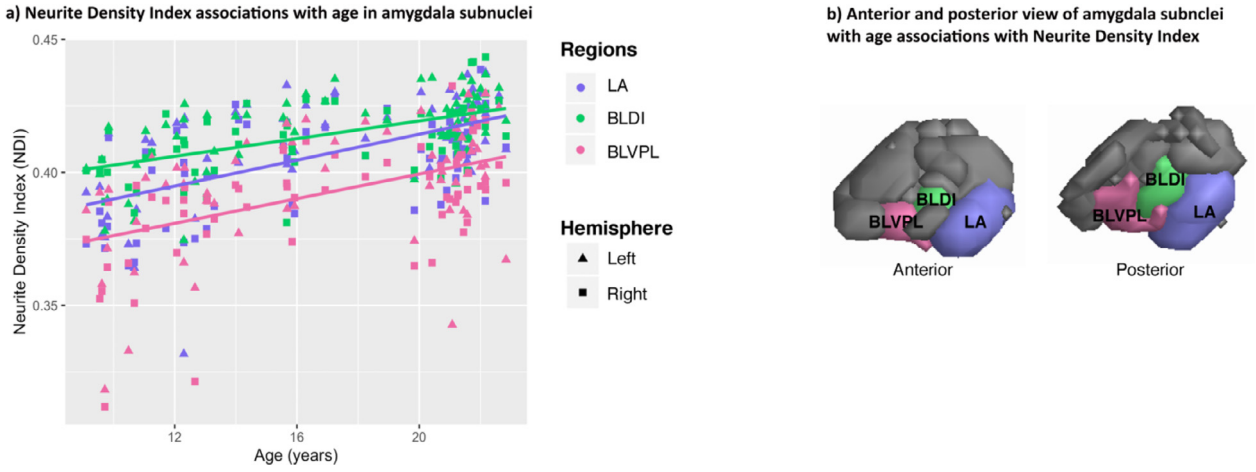

Fig. 2. Age-related increases in Neurite Density Index (NDI) found in (a) 3 of the amygdala subnuclei: lateral (LA), dorsal and intermediate division of its basolateral nucleus (BLDI), and ventral division of the basolateral nucleus and paralaminar nucleus (BLVPL) plotted by age (years) and collapsed across hemispheres. Lines represent predicted age associations from each respective model. The location of the 3 subnuclei within the left amygdala are shown in b.

ODI along the anterior commissure and NDI along both hemispheres of the ventral amygdalofugal pathway, cingulum, and uncinate fasciculus. The mean and standard deviation NDI at each point along these tracts are shown in **Supplemental Fig. 9**. The standardized betas for the age-effects of NDI at each point from our multi-level models are shown in Fig. 4. Results showed significant age-by-point interaction for NDI for the anterior commissure (ω^2 = 0.07, F(26, 1534) = 5.33, p < 0.0001), left and right uncinate fasciculus (left: ω^2 = 0.07, F(11, 649) = 5.33, p < 0.0001; right: ω^2 = 0.09, F(14, 826) = 6.59, p < 0.0001), right ventral amygdalofugal pathway (ω^2 = 0.02, F(13, 767) = 2.53, p < 0.005), left and right cingulum (left: ω^2 = 0.02, F(37, 2183) = 2.07, p < 0.0005; right: ω^2 = 0.04, F(40, 2360) = 3.65, p < 0.0001). However, the age effects did not significantly differ with NDI along the left ventral amygdalofugal (ω^2 = 0.007, F(15, 885) = 1.42, p = 0.15). Age effects also did not significantly differ with ODI along the anterior commissure (ω^2 = 0.002, F(26, 1534) = 1.165, p = 0.26). All tracts displayed stronger age-effects with NDI in the frontal and temporal regions and the ventral amygdalofugal pathway also displayed stronger age-effects with NDI in the diencephalic region (Fig. 4).

4. Discussion

Using cutting-edge structural segmentation of the amygdala coupled with NODDI, our study is the first to examine microstructural properties of amygdala subnuclei across adolescence. Additionally, our paper is the first to elucidate the microstructural properties of the ventral amygdalofugal pathway in children and adolescents. In addition to replicating increases in neurite density values with age (i.e. NDI) for the entire amygdala, we expanded these findings to show that neurite density increases are particularly seen in basolateral nuclei, including the LA, BLDI, and BLVPL. Of the three primary amygdala efferent white matter pathways, we found age-related increases in NDI for the ventral amygdalofugal pathway and increases in NDI and ODI in the anterior commissure. We also replicated previous research that also found age-

Table 2
Age, sex, and interaction associations with NODDI measures within the amygdala and its subnuclei. Unstandardized and standardized (std.) estimates and standard error (SE), FDR-corrected p values (p), marginalized R^2 and conditional R^2 or R^2 and R^2 adjusted are shown. Model estimates are reported while adjusting for BMIz, mother's education, race, hemisphere, motion (RMS), and volume of the respective region of interest.

	NDI					ODI				
	beta	*SE*	*std. beta*	*std. SE*	*FDR p*	*beta*	*SE*	*std. beta*	*std. SE*	*FDR p*
LA										
age	0.002	0.001	0.54	0.15	**0.009**	0.003	0.002	0.30	0.16	0.19
sex	-0.005	0.009	-0.02	0.22	0.91	-0.04	0.02	-0.46	0.23	0.84
age-by-sex	0.001	0.001	0.15	0.22	0.84	0.003	0.002	0.28	0.23	0.84
Marginal R^2, Conditional R^2	0.395, 0.832	0.162, 0.454								
BLDI										
age	0.002	0.0004	0.55	0.14	**0.008**	0.004	0.002	0.34	0.16	0.13
sex	-0.006	0.006	-0.33	0.21	0.84	-0.04	0.03	-0.15	0.23	0.84
age-by-sex	0.0002	0.0006	0.08	0.21	0.84	0.004	0.003	0.31	0.23	0.84
Marginal R^2, Conditional R^2	0.406, 0.769	0.180, 0.506								
BM										
age	0.0009	0.001	0.25	0.17	0.27	-0.001	0.002	-0.07	0.19	0.74
sex	-0.0001	0.008	-0.29	0.24	0.99	0.002	0.03	-0.04	0.26	0.99
age-by-sex	-0.0006	0.001	-0.17	0.24	0.84	-0.001	0.003	-0.04	0.26	0.87
Marginal R^2, Conditional R^2	0.157, 0.570	0.111, 0.708								
CEN										
age	0.001	0.001	0.30	0.17	0.20	-0.002	0.002	-0.142	0.19	0.62
sex	-0.009	0.01	-0.16	0.24	0.87	-0.02	0.03	0.230	0.26	0.87
age-by-sex	0.001	0.001	0.14	0.24	0.84	0.005	0.003	0.387	0.26	0.84
Marginal R^2, Conditional R^2	0.203, 0.680	0.130, 0.730								
CMN										
age	-0.001	0.001	-0.10	0.17	0.64	-0.001	0.002	-0.10	0.17	0.64
sex	-0.001	0.018	0.34	0.24	0.99	0.006	0.02	-0.15	0.25	0.99
age-by-sex	0.002	0.002	0.22	0.24	0.84	-0.002	0.003	-0.16	0.25	0.84
Marginal R^2, Conditional R^2	0.141, 0.520	0.148, 0.658								
BLVPL										
age	0.002	0.001	0.43	0.14	**0.03**	0.0005	0.002	0.04	0.19	0.83
sex	-0.008	0.009	-0.21	0.21	0.87	0.02	0.03	0.18	0.27	0.94
age-by-sex	0.0005	0.001	0.10	0.21	0.84	-0.001	0.003	-0.07	0.28	0.85
Marginal R^2, Conditional R^2	0.351, 0.653	0.041, 0.672								
ATA										
age	0.003	0.002	0.22	0.16	0.29	0.005	0.002	0.37	0.16	0.12
sex	0.02	0.03	0.19	0.23	0.91	0.001	0.03	-0.18	0.24	0.99
age-by-sex	-0.001	0.003	-0.06	0.23	0.85	-0.002	0.003	-0.11	0.23	0.84
Marginal R^2, Conditional R^2	0.117, 0.378	0.179, 0.577								
ASTA										
age	0.002	0.001	0.26	0.17	0.27	-0.002	0.001	-0.26	0.18	0.27
sex	-0.016	0.01	-0.25	0.25	0.84	-0.03	0.02	-0.16	0.25	0.84
age-by-sex	0.001	0.002	0.18	0.25	0.84	0.003	0.002	0.35	0.25	0.84
Marginal R^2, Conditional R^2	0.145, 0.620	0.151, 0.674								
AAA										
age	-0.001	0.002	-0.10	0.18	0.66	-0.002	0.002	-0.16	0.17	0.53
sex	-0.005	0.03	0.07	0.25	0.99	-0.03	0.03	-0.13	0.23	0.84
age-by-sex	0.001	0.003	0.09	0.25	0.84	0.003	0.003	0.23	0.23	0.84
Marginal R^2, Conditional R^2	0.123, 0.661	0.129, 0.488								
Whole Amygdala										
age	0.001	0.001	0.40	0.16	0.07	0.0009	0.001	0.14	0.19	0.62
sex	-0.003	0.008	0.04	0.23	0.95	-0.02	0.02	-0.34	0.27	0.84
age-by-sex	0.0005	0.001	0.14	0.23	0.84	0.002	0.002	0.24	0.27	0.84
Marginal R^2, Conditional R^2	0.318, 0.729	0.065, 0.627								

related increases of NDI in the entire bundles of the uncinate fasciculus and the cingulum (Lynch et al., 2020; Mah et al., 2017). However, we also elaborated upon these findings to show that age-related increases in NDI along these tracts is most robust at the tail end of these tracts that integrates with the frontal and temporal cortical gray matter. Together, these results suggest neurite cellular architecture within the amygdala, as well as the axonal white matter projections carrying amygdala fibers, continue to mature across adolescence.

Our results also show that microstructural composition of the amygdala varies across age in the lateral nucleus (LA), dorsal and intermediate divisions of the basolateral nucleus (BLDI), and the ventral division of the basolateral nucleus and paralaminar nucleus (BLVPL). Histological results based on a sample of 52 participants between the ages 2 to 48 years show that there is a ~11% increase in the number of mature neurons in the whole amygdala (Avino et al., 2018), but this increase is primarily accounted for by a significant increase in mature neurons in the basal nucleus (30%) as well as a 3% increase in the number of mature neurons in the lateral nucleus, albeit not significant. Additionally, Avino et al. (2018) found an age-related decrease in the number of immature neurons within the paralaminar nucleus, which signifies changes in neuronal composition within this region with age. The histological data from Avino et al. (2018), along with research indicating that the transition from immature to mature neurons is marked by dendritic arborization and axonal growth (Spitzer, 2006), allow us to hypothesize that during adolescent development, the age-related pattern in neurite density we found in the LA, BLDI, and BLVPL could be a result of changes in the number of immature versus mature neurons present in these subnuclei. Furthermore, animal literature on gene expression patterns show that in adult rats the lateral and basal nuclei express more genes than the central nucleus that are involved in axonogenesis, neuron development,

Table 3
Associations of age, sex, and their interaction for NDI and ODI of white matter bundles. Unstandardized and standardized (std.) estimates and standard error (SE), FDR-corrected p values (p), marginalized R^2 and conditional R^2 or R^2 and R^2 adjusted are shown. Model estimates are reported while adjusting for BMIz, mother's education, race, hemisphere, motion (RMS), and streamline number for the respective track of interest.

	NDI					ODI				
	beta	*SE*	*std. beta*	*std. SE*	*FDR p*	*beta*	*SE*	*std. beta*	*std. SE*	*FDR p*
Ventral amygdalofugal pathway										
age	0.002	0.0007	0.52	0.16	**0.008**	0.0009	0.0005	0.26	0.15	0.17
sex	-0.003	0.009	-0.01	0.23	0.97	-0.007	0.0073	-0.26	0.22	0.97
age-by-sex	0.0004	0.0009	0.1	0.23	0.84	0.0004	0.0008	0.1	0.22	0.84
Marginal R^2, Conditional R^2	0.350, 0.902				0.297, 0.688					
Uncinate fasciculus										
age	0.0024	0.0007	0.42	0.12	**0.004**	0.0008	0.0004	0.31	0.13	0.053
sex	-0.007	0.009	0.12	0.17	0.97	0.003	0.005	-0.33	0.18	0.97
age-by-sex	0.0013	0.001	0.22	0.17	0.83	-0.0009	0.0005	-0.32	0.18	0.83
Marginal R^2, Conditional R^2	0.613, 0.917				0.439, 0.650					
Fornix										
age	0.001	0.001	0.28	0.16	0.17	0.0005	0.0004	0.17	0.15	0.37
sex	-0.003	0.01	0.17	0.23	0.97	0.0008	0.006	0.02	0.22	0.97
age-by-sex	0.001	0.001	0.19	0.23	0.83	-0.0001	0.0006	-0.02	0.22	0.96
Marginal R^2, Conditional R^2	0.252, 0.750				0.269, 0.601					
Stria terminalis										
age	0.0009	0.001	0.14	0.16	0.43	0.0005	0.0005	0.12	0.13	0.43
sex	-0.001	0.01	0.33	0.23	0.97	0.01	0.01	0.41	0.19	0.97
age-by-sex	0.001	0.001	0.21	0.22	0.83	-0.0005	0.0008	-0.13	0.19	0.83
Marginal R^2, Conditional R^2	0.321, 0.771				0.337, 0.508					
Cingulum										
age	0.003	0.001	0.60	0.14	**0.001**	-0.0003	0.0004	-0.12	0.15	0.43
sex	-0.002	0.01	0.20	0.2	0.97	-0.004	0.005	-0.33	0.21	0.97
age-by-sex	0.001	0.001	0.18	0.2	0.83	0.00003	0.0006	0.01	0.21	0.96
Marginal R^2, Conditional R^2	0.451, 0.834				0.315, 0.616					
Anterior commissure										
age	0.002	0.001	0.51	0.16	**0.01**	0.001	0.0005	0.29	0.13	**0.03**
sex	-0.013	0.01	-0.06	0.23	0.38	-0.006	0.007	-0.42	0.19	0.40
age-by-sex	0.001	0.001	0.34	0.23	0.29	-0.0002	0.0007	-0.06	0.19	0.77
R^2, R^2 adjusted	0.456, 0.334				0.633, 0.551					

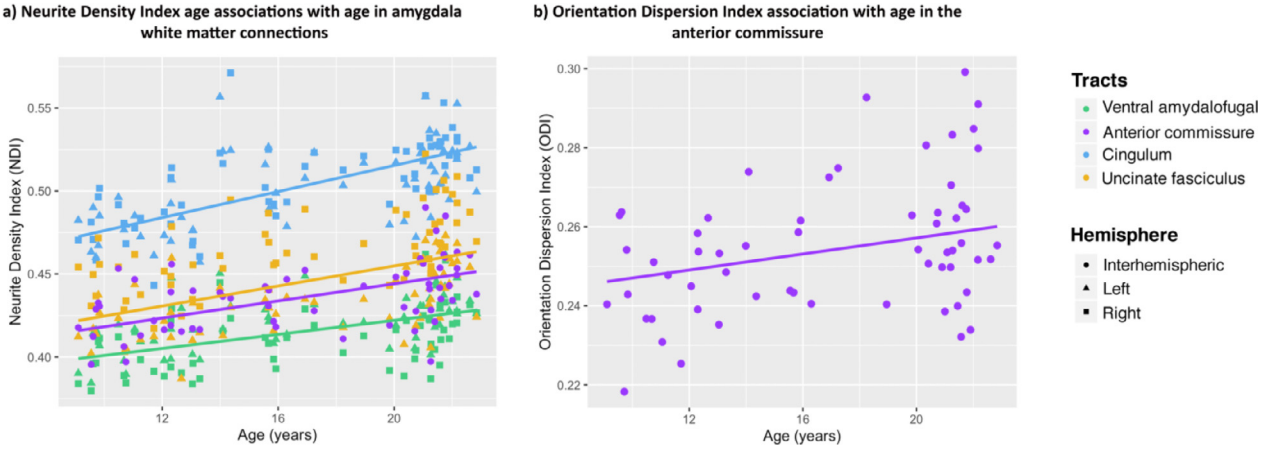

Fig. 3. (a) Age-related increases in Neurite Density Index (NDI) found in the ventral amygdalofugal pathway, anterior commissure, cingulum, and uncinate fasciculus plotted by age and collapsed across hemispheres. (b) Age-related increase in Orientation Dispersion Index found only in the anterior commissure plotted by age. Lines represent predicted age association from each respective model.

neuron projection development, and neuron projection morphogenesis (Partin et al., 2013). In combination with the gene expression data, the lateral and basal nuclei in particular, through their involvement in neurite maturation, may be important components to amygdala circuitry development.

Through our cutting-edge tractography methods we were able to delineate and obtain both DTI and NODDI metrics from several white matter connections to the amygdala. Furthermore, our paper is the first to reveal both DTI and NODDI values of the ventral amygdalofugal pathway. Our white matter analyzes revealed age-associated increases in NDI of amygdalar connections to the uncinate fasciculus, cingulum, ventral amygdalofugal pathway, and anterior commissure, signifying increasing fiber packing density in these white matter tracts (Lebel and Deoni, 2018; Zhang et al., 2012). Previous studies showing increases in neurite density in other white matter tracts have suggested that both fiber diameter and myelination during development could contribute to these increases in NDI (Chang et al., 2015). Particularly interesting is that our along-tract analyzes reveal the superficial white matter frontal and temporal regions of these tracts have the strongest age associations with NDI, suggesting that those regions specifically are displaying the most increases in fiber packing density and/or myelination in our age range. In addition to increases in NDI, the anterior commissure also dis-

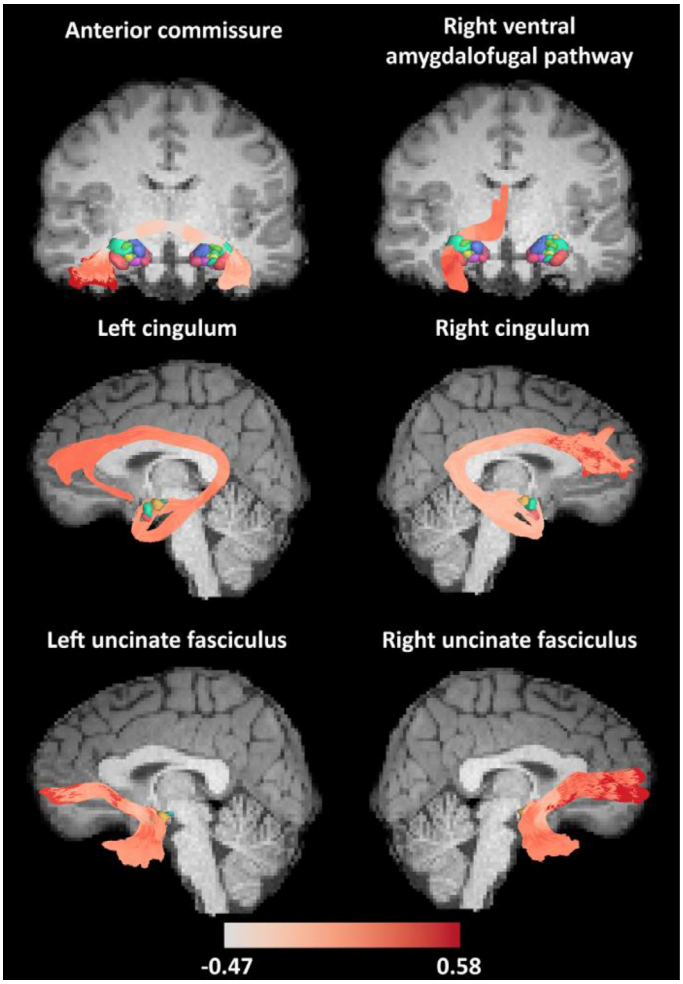

Fig. 4. Age-associations (standardized betas) with Neurite Density Index (NDI) at each point along the tracts as seen on a representative subject's tracts and structural image with 3D rendering of the amygdala subnuclei. Darker red on the color bar indicates larger standardized beta values.

played overall increases of ODI with age. However, whereas age effects of NDI were most robust at the end of the anterior commissure, ODI associations with age were similar along the length of the tract, suggesting both the microstructural, and thus the potential underlying biological, properties may differ in the body versus the end portions of the tract. While diffusion MRI is unable to detect the exact microbiology, it is important to note that it is estimated that a single $2mm^3$ white matter voxel is comprised of not only myelinated and non-myelinated axons, but a large number of glial cells, including a large proportion of oligodendrocytes, and to a lesser degree astrocytes and microglial cells (Walhovd et al., 2014). Thus, it is feasible that increases in NDI may relate to increased fiber packing density or myelination of the anterior commissure near temporal regions, whereas the increase in ODI averaged across the track may be picking up on changes in dispersion due to increases in density or size of support cells within the anterior commissure. Alternatively, given that commissural fibers tend to mature earlier than other white matter tracts, with diffusion metrics of maturation peaking in the early 20's (before age related decreases are noted) (Dubois et al., 2014; Lebel et al., 2012), it is feasible that increases in ODI may also be reflective of early age-related disruptions in myelin axon fibers in portions of the anterior commissure that may begin as early as the second decade of life (Chang et al., 2015). Additional human longitudinal studies and animal models using both histology and high-resolution diffusion MRI are necessary in order to test these potential hypotheses.

Combining amygdala and white matter findings in the same individuals provides more information regarding specific amygdala related neural circuitry that may continue to develop across adolescence. The lateral and basal nuclei are involved in learning, memory, emotional processing, sensory processing, social behaviors, and reward processing (Janak and Tye, 2015; LeDoux, 2007; Sah et al., 2003; Yang and Wang, 2017; Yizhar and Klavir, 2018). Both nuclei have extensive connections to the prefrontal cortex, temporal lobe, nucleus accumbens, and striatum (Sah et al., 2003). The uncinate fasciculus has connections to the orbitofrontal cortex and Brodmann area 10 as well as temporal lobe and has been found to be involved in social-emotional processing (Olson et al., 2015; Von Der Heide et al., 2013). The ventral amygdalofugal pathway connects the amygdala to the hypothalamus, nucleus accumbens, thalamus, and bed nucleus of the stria terminalis (Kamali et al., 2016) and is thought to be involved in generating emotional responses from the amygdala. The cingulum connects the orbitofrontal and cingulate cortex to the temporal pole and is involved in executive function, attention, and emotion processing (Bubb et al., 2018). The anterior commissure has connections to the temporal pole and is involved in attention (Lavrador et al., 2019). Altogether, our results suggest that adolescent development is a critical period for the maturation of neural circuitry involving amygdala subnuclei and white matter related to learning how to process social and emotional cues and responding to them. Our along-tract analyses also suggest that the maturation of the neural circuitry may not be exclusive to amygdala subnuclei and white matter. The uncinate fasciculus and cingulum connect the amygdala to frontal and temporal regions of the brain and these regions are where we saw the strongest age-effects with NDI. The anterior commissure connects the amygdala with the temporal lobe, and we saw large age-effects with NDI within the temporal region of the anterior commissure. Lastly, the ventral amygdalofugal pathway connects the amygdala to several structures of the diencephalon, which is where we also saw strong age effects. Overall, these results suggest that along with the amygdala subnuclei and white matter tracts, the grey matter regions that are connected to the amygdala via our tracts of interest may also be maturing at the same time, further promoting the maturation of emotional and social neural circuitry.

A few limitations of the current study should be noted. First, our final sample size had 61 participants, limiting our ability power to detect smaller effects. For example, despite a number of known sex differences in amygdala development (Giedd et al., 1996; Herting et al., 2018), we did not find a significant difference in age relationships stratified by sex. We were also unable to examine the influence of pubertal development on DTI and NODDI measures because the data for this analysis came from two study samples with various ages (8–18 years and 19–23 years), where individuals over the age of 18 were not asked about pubertal maturation. Thus, future larger studies are needed to assess if pubertal maturation may play a role in any of the age-related associations seen in the current study. Additionally, there are a few limitations of diffusion MRI, such as acquisition and analysis methods, (Jones et al., 2013) which can affect the anatomical accuracy of fiber tractography (Schilling et al., 2019; Thomas et al., 2014). Furthermore, modeling diffusion MRI with NODDI requires using specific fixed parameters which introduce modeling assumptions that can be addressed with additional shells (Guerrero et al., 2019). Finally, co-registered T1- and T2-weighted structural data may offer useful additional constraints for an extended NODDI model, particularly for myelin content estimation (Glasser and Van Essen, 2011) although the construction and validation of such as multimodal model is beyond the scope of this current work. Similarly, other studies have reported using DTI metrics to segment the amygdala into 3 larger subregions (Solano-Castiella et al., 2010), suggesting future research may consider if the integration of NODDI estimates may complement T1/T2-derived MRI amygdala segmentation atlases, such as the CIT168. Future studies optimizing acquisition and analysis meth-

ods should consider tackling these methodological questions. Our study is also limited in that it is cross-sectional in nature. Longitudinal studies are needed to confirm the developmental changes in microstructural properties of the amygdala as well as its affiliated white matter pathways across childhood and adolescence within individual subjects.

5. Conclusion

This is the first study to utilize NODDI to assess neurite density of amygdala subnuclei across adolescence. Overall, our research emphasizes that specific age-related differences exist in the microstructural properties of key basolateral amygdala subnuclei as well as along two key white matter tracts of the amygdala (ventral amygdalofugal pathway, anterior commissure). As these regions have been involved in associative emotional learning, future research is needed to determine if age-related and/or individual differences in the development of these microstructural properties link to typical and/or atypical social and emotional functioning.

Declaration of Competing Interest

None

Credit authorship contribution statement

Anisa Azad: Conceptualization, Formal analysis, Writing – original draft, Validation, Visualization. **Ryan P. Cabeen:** Methodology, Visualization, Writing – review & editing. **Farshid Sepehrband:** Methodology, Writing – review & editing. **Robert Kim:** Data curation, Writing – review & editing. **Claire E. Campbell:** Data curation, Methodology, Writing – original draft. **Kirsten Lynch:** Methodology, Writing – review & editing. **J. Michael Tyszka:** Methodology, Writing – review & editing. **Megan M. Herting:** Funding acquisition, Conceptualization, Investigation, Methodology, Supervision, Project administration, Writing – original draft.

Data availability statement

Due to the nature of the study, the data are not publicly available as participants of this study did not agree for their data to be shared publicly. The data that support the findings of this study are available on request from the corresponding author, MMH, but will require a formal sharing agreement.

Funding

Financial support was provided by the National Institutes of Health under award numbers: K01 MH1087610, R03 HD090308, the Neuroimaging Core of a Conte Center grant (5P50MH094258), P41EB015922, and the Predoctoral Training Grant in Environmental Genomics (T32ES013678); the Diabetes & Obesity Research Institute (DORI) with funding from the Stewart Clifton Endowment; and the Southern California Clinical and Translational Science Institute (SC CTSI) Pilot Funding Program grant UL1TR001855. The funding sources had no involvement in study design; data collection, analysis, and interpretation; writing the report; or the decision to submit the article for publication. The content is solely the responsibility of the authors and does not necessarily represent the official views of the DORI or the Stewart Clifton Endowment.

Acknowledgments

The authors thank all participating individuals and families in these studies. In addition, we would like to acknowledge Dr. Mimi Kim, Norma Martinez, Heather Ross, Christina Koppin, Michelle Canales, Kimberly Felix, Adam Mezher, and Eva Gabor for assisting with participant recruitment and data collection as part of various studies that contributed data to this project. Computation for the work described in this paper was supported by the University of Southern California's Center for High-Performance Computing (hpcc.usc.edu).

Supplementary materials

Supplementary material associated with this article can be found, in the online version, at doi:10.1016/j.neuroimage.2021.118489.

References

Abivardi, A., Bach, D.R., 2017. Deconstructing white matter connectivity of human amygdala nuclei with thalamus and cortex subdivisions *in vivo*. Hum Brain Mapp. 38, 3927–3940.

Amunts, K., Kedo, O., Kindler, M., Pieperhoff, P., Mohlberg, H., Shah, N.J., Habel, U., Schneider, F., Zilles, K., 2005. Cytoarchitectonic mapping of the human amygdala, hippocampal region and entorhinal cortex: intersubject variability and probability maps. Anat. Embryol. (Berl) 210, 343–352.

Assaf, Y., Pasternak, O., 2008. Diffusion tensor imaging (DTI)-based white matter mapping in brain research: a review. J. Mol. Neurosci. 34, 51–61.

Avants, B.B., Duda, J.T., Zhang, H., Gee, J.C., 2007. Multivariate normalization with symmetric diffeomorphisms for multivariate studies. Med. Image Comput. Comput. Assist. Interv. 10, 359–366.

Avino, T.A., Barger, N., Vargas, M.V., Carlson, E.L., Amaral, D.G., Bauman, M.D., Schumann, C.M., 2018. Neuron numbers increase in the human amygdala from birth to adulthood, but not in autism. Proc. Natl. Acad. Sci. USA. 115, 3710–3715.

Backhausen, L.L., Herting, M.M., Buse, J., Roessner, V., Smolka, M.N., Vetter, N.C., 2016. Quality control of structural MRI images applied using freesurfer-a hands-on workflow to rate motion artifacts. Front Neurosci. 10, 558.

Bates, D, Mächler, M, Bolker, B, Walker, S, 2015. Fitting Linear Mixed-Effects Models Using lme4. Journal of Statistical Software 67 (1), 1–48.

Behrens, T.E., Berg, H.J., Jbabdi, S., Rushworth, M.F., Woolrich, M.W., 2007. Probabilistic diffusion tractography with multiple fibre orientations: What can we gain? Neuroimage 34, 144–155.

Benes, F.M., Turtle, M., Khan, Y., Farol, P., 1994. Myelination of a key relay zone in the hippocampal formation occurs in the human brain during childhood, adolescence, and adulthood. Arch. Gen. Psychiatry 51, 477–484.

Bubb, E.J., Metzler-Baddeley, C., Aggleton, J.P., 2018. The cingulum bundle: anatomy, function, and dysfunction. Neurosci Biobehav Rev 92, 104–127.

Cabeen, R., Laidlaw, D., Toga, A., 2018. Quantitative Imaging toolkit: software for interactive 3D visualization, data exploration, and computational analysis of neuroimaging datasets. Proc. Int. Soc. Mag. Resonance Med. (ISMRM) 2018, 2854.

Cabeen, R.P., Bastin, M.E., Laidlaw, D.H., 2016. Kernel regression estimation of fiber orientation mixtures in diffusion MRI. Neuroimage 127, 158–172.

Cabeen, R.P., Toga, A.W., 2020. Reinforcement tractography: a hybrid approach for robust segmentation of complex fiber bundles. In: Proceedings of the IEEE 17th International Symposium on Biomedical Imaging (ISBI) pp. 999-103.

Campbell, C.E., Mezher, A.F., Eckel, S.P., Tyszka, J.M., Pauli, W.M., Nagel, B.J., Herting, M.M., 2021. Restructuring of amygdala subregion apportion across adolescence. Dev. Cogn. Neurosci. 48, 100883.

Caruyer, E., Lenglet, C., Sapiro, G., Deriche, R., 2013. Design of multishell sampling schemes with uniform coverage in diffusion MRI. Magn. Reson. Med. 69, 1534–1540.

Catani, M., Thiebaut de Schotten, M., 2008. A diffusion tensor imaging tractography atlas for virtual *in vivo* dissections. Cortex 44, 1105–1132.

Chang, Y.S., Owen, J.P., Pojman, N.J., Thieu, T., Bukshpun, P., Wakahiro, M.L., Berman, J.I., Roberts, T.P., Nagarajan, S.S., Sherr, E.H., Mukherjee, P., 2015. White matter changes of neurite density and fiber orientation dispersion during human brain Maturation. PLoS One 10, e0123656.

Chareyron, L.J., Banta Lavenex, P., Amaral, D.G., Lavenex, P., 2011. Stereological analysis of the rat and monkey amygdala. J. Comparat. Neurol. 519, 3218–3239.

Colby, J.B., Soderberg, L., Lebel, C., Dinov, I.D., Thompson, P.M., Sowell, E.R., 2012. Along-tract statistics allow for enhanced tractography analysis. Neuroimage 59, 3227–3242.

Dubois, J., Dehaene-Lambertz, G., Kulikova, S., Poupon, C., Huppi, P.S., Hertz-Pannier, L., 2014. The early development of brain white matter: a review of imaging studies in fetuses, newborns and infants. Neuroscience 276, 48–71.

Edwards, L.J., Pine, K.J., Ellerbrock, I., Weiskopf, N., Mohammadi, S., 2017. NODDI-DTI: estimating neurite orientation and dispersion parameters from a diffusion tensor in healthy white matter. Front Neurosci. 11, 720.

Fischl, B., Salat, D.H., Busa, E., Albert, M., Dieterich, M., Haselgrove, C., van der Kouwe, A., Killiany, R., Kennedy, D., Klaveness, S., Montillo, A., Makris, N., Rosen, B., Dale, A.M., 2002. Whole brain segmentation: automated labeling of neuroanatomical structures in the human brain. Neuron 33, 341–355.

Fukutomi, H., Glasser, M.F., Murata, K., Akasaka, T., Fujimoto, K., Yamamoto, T., Autio, J.A., Okada, T., Togashi, K., Zhang, H., Van Essen, D.C., Hayashi, T., 2019. Diffusion tensor model links to neurite orientation dispersion and density imaging at high b-value in cerebral cortical gray matter. Scient. Rep. 9, 12246.

Geeraert, B.L., Lebel, R.M., Lebel, C., 2019. A multiparametric analysis of white matter maturation during late childhood and adolescence. Hum Brain Mapp. 40, 4345–4356.

Genc, S., Malpas, C.B., Holland, S.K., Beare, R., Silk, T.J., 2017. Neurite density index is sensitive to age related differences in the developing brain. Neuroimage 148, 373–380.
Gershon, R.C., Wagster, M.V., Hendrie, H.C., Fox, N.A., Cook, K.F., Nowinski, C.J., 2013. NIH toolbox for assessment of neurological and behavioral function. Neurology 80, S2–S6.
Giedd, J.N., Vaituzis, A.C., Hamburger, S.D., Lange, N., Rajapakse, J.C., Kaysen, D., Vauss, Y.C., Rapoport, J.L., 1996. Quantitative MRI of the temporal lobe, amygdala, and hippocampus in normal human development: ages 4–18 years. J. Comp. Neurol. 366, 223–230.
Glasser, M.F., Van Essen, D.C., 2011. Mapping human cortical areas *in vivo* based on myelin content as revealed by T1- and T2-weighted MRI. J. Neurosci. 31, 11597–11616.
Grussu, F., Schneider, T., Zhang, H., Alexander, D.C., Wheeler-Kingshott, C.A., 2015. Neurite orientation dispersion and density imaging of the healthy cervical spinal cord *in vivo*. Neuroimage 111, 590–601.
Guerrero, J.M., Adluru, N., Bendlin, B.B., Goldsmith, H.H., Schaefer, S.M., Davidson, R.J., Kecskemeti, S.R., Zhang, H., Alexander, A.L., 2019. Optimizing the intrinsic parallel diffusivity in NODDI: an extensive empirical evaluation. PLoS One 14, e0217118.
Heilbronner, S.R., Haber, S.N., 2014. Frontal cortical and subcortical projections provide a basis for segmenting the cingulum bundle: implications for neuroimaging and psychiatric disorders. J. Neurosci. 34, 10041–10054.
Herting, M.M., Azad, A., Kim, R., Tyszka, J.M., Geffner, M.E., Kim, M.S., 2020. Brain differences in the prefrontal cortex, amygdala, and hippocampus in youth with congenital adrenal hyperplasia. J. Clin. Endocrinol. Metab. 105, 1098–1111.
Herting, M.M., Johnson, C., Mills, K.L., Vijayakumar, N., Dennison, M., Liu, C., Goddings, A.L., Dahl, R.E., Sowell, E.R., Whittle, S., Allen, N.B., Tamnes, C.K., 2018. Development of subcortical volumes across adolescence in males and females: a multisample study of longitudinal changes. Neuroimage 172, 194–205.
Ho, N.F., Li Hui Chong, P., Lee, D.R., Chew, Q.H., Chen, G., Sim, K., 2019. The amygdala in schizophrenia and bipolar disorder: a synthesis of structural MRI, diffusion tensor imaging, and resting-state functional connectivity findings. Harv. Rev. Psychiatry 27, 150–164.
Jalbrzikowski, M., Larsen, B., Hallquist, M.N., Foran, W., Calabro, F., Luna, B., 2017. Development of white matter microstructure and intrinsic functional connectivity between the amygdala and ventromedial prefrontal cortex: associations with anxiety and depression. Biol. Psychiatry 82, 511–521.
Janak, P.H., Tye, K.M., 2015. From circuits to behavior in the amygdala. Nature 517, 284–292.
Jenkinson, M., 2003. Fast, automated, N-dimensional phase-unwrapping algorithm. Magn. Reson. Med. 49, 193–197.
Jenkinson, M., Beckmann, C.F., Behrens, T.E., Woolrich, M.W., Smith, S.M., 2012. FSL. Neuroimage 62, 782–790.
Jones, D.K., Knosche, T.R., Turner, R., 2013. White matter integrity, fiber count, and other fallacies: the do's and don'ts of diffusion MRI. Neuroimage 73, 239–254.
Kamali, A., Sair, H.I., Blitz, A.M., Riascos, R.F., Mirbagheri, S., Keser, Z., Hasan, K.M., 2016. Revealing the ventral amygdalofugal pathway of the human limbic system using high spatial resolution diffusion tensor tractography. Brain Struct. Funct. 221, 3561–3569.
Kessler, R.C., Berglund, P., Demler, O., Jin, R., Merikangas, K.R., Walters, E.E., 2005. Lifetime prevalence and age-of-onset distributions of DSM-IV disorders in the national comorbidity survey replication. Arch. Gen. Psychiatry 62, 593–602.
Kim, M.J., Loucks, R.A., Palmer, A.L., Brown, A.C., Solomon, K.M., Marchante, A.N., Whalen, P.J., 2011. The structural and functional connectivity of the amygdala: from normal emotion to pathological anxiety. Behav. Brain Res. 223, 403–410.
Kuczmarski, R.J., Ogden, C.L., Guo, S.S., Grummer-Strawn, L.M., Flegal, K.M., Mei, Z., Wei, R., Curtin, L.R., Roche, A.F., Johnson, C.L., 2002. 2000 CDC growth charts for the United States: methods and development. Vital Health Stat. 11, 1–190.
Kullmann, S., Schweizer, F., Veit, R., Fritsche, A., Preissl, H., 2015. Compromised white matter integrity in obesity. Obes. Rev. 16, 273–281.
Lavrador, J.P., Ferreira, V., Lourenco, M., Alexandre, I., Rocha, M., Oliveira, E., Kailaya–Vasan, A., Neto, L., 2019. White-matter commissures: a clinically focused anatomical review. Surg. Radiol. Anat. 41, 613–624.
Lebel, C., Deoni, S., 2018. The development of brain white matter microstructure. Neuroimage 182, 207–218.
Lebel, C., Gee, M., Camicioli, R., Wieler, M., Martin, W., Beaulieu, C., 2012. Diffusion tensor imaging of white matter tract evolution over the lifespan. Neuroimage 60, 340–352.
Lebow, M.A., Chen, A., 2016. Overshadowed by the amygdala: the bed nucleus of the stria terminalis emerges as key to psychiatric disorders. Mol. Psychiatry 21, 450–463.
LeDoux, J., 2007. The amygdala. Curr. Biol. 17, R868–R874.
Lovblad, K.O., Schaller, K., Vargas, M.I., 2014. The fornix and limbic system. Semin Ultrasound CT MR 35, 459–473.
Lynch, K.M., Cabeen, R.P., Toga, A.W., Clark, K.A., 2020. Magnitude and timing of major white matter tract maturation from infancy through adolescence with NODDI. Neuroimage 212, 116672.
Mah, A., Geeraert, B., Lebel, C., 2017. Detailing neuroanatomical development in late childhood and early adolescence using NODDI. PLoS One 12, e0182340.
Noback, C.R., Ruggiero, D.A., Demarest, R.J., Strominger, N.L., 2005. The Human Nervous System: Structure and Function. Humana Press.
Olson, I.R., Von Der Heide, R.J., Alm, K.H., Vyas, G., 2015. Development of the uncinate fasciculus: Implications for theory and developmental disorders. Dev. Cogn. Neurosci. 14, 50–61.
Orsi, G., Perlaki, G., Kovacs, N., Aradi, M., Papp, Z., Karadi, K., Szalay, C., Karadi, Z., Lenard, L., Tenyi, T., Plozer, E., Gabriel, R., Nagy, F., Doczi, T., Komoly, S., Jokeit, H., Schwarcz, A., Janszky, J., 2011. Body weight and the reward system: the volume of the right amygdala may be associated with body mass index in young overweight men. Brain Imaging Behav. 5, 149–157.
Partin, A.C., Hosek, M.P., Luong, J.A., Lella, S.K., Sharma, S.A., Ploski, J.E., 2013. Amygdala nuclei critical for emotional learning exhibit unique gene expression patterns. Neurobiol. Learn Mem. 104, 110–121.
Pascalau, R., Popa Stanila, R., Sfrangeu, S., Szabo, B., 2018. Anatomy of the limbic white matter tracts as revealed by fiber dissection and tractography. World Neurosurg. 113, e672–e689.
Pauli, W.M., Nili, A.N., Tyszka, J.M., 2018. A high-resolution probabilistic *in vivo* atlas of human subcortical brain nuclei. Sci. Data 5, 180063.
Phelps, E.A., LeDoux, J.E., 2005. Contributions of the amygdala to emotion processing: from animal models to human behavior. Neuron 48, 175–187.
Reuter, M., Schmansky, N.J., Rosas, H.D., Fischl, B., 2012. Within-subject template estimation for unbiased longitudinal image analysis. Neuroimage 61, 1402–1418.
Roalf, D.R., Quarmley, M., Elliott, M.A., Satterthwaite, T.D., Vandekar, S.N., Ruparel, K., Gennatas, E.D., Calkins, M.E., Moore, T.M., Hopson, R., Prabhakaran, K., Jackson, C.T., Verma, R., Hakonarson, H., Gur, R.C., Gur, R.E., 2016. The impact of quality assurance assessment on diffusion tensor imaging outcomes in a large-scale population-based cohort. Neuroimage 125, 903–919.
Rus, O.G., Reess, T.J., Wagner, G., Zimmer, C., Zaudig, M., Koch, K., 2017. Functional and structural connectivity of the amygdala in obsessive-compulsive disorder. Neuroimage Clin. 13, 246–255.
Sah, P., Faber, E.S., Lopez De Armentia, M., Power, J., 2003. The amygdaloid complex: anatomy and physiology. Physiol. Rev. 83, 803–834.
Saygin, Z.M., Osher, D.E., Koldewyn, K., Martin, R.E., Finn, A., Saxe, R., Gabrieli, J.D., Sheridan, M., 2015. Structural connectivity of the developing human amygdala. PLoS One 10, e0125170.
Schilling, K.G., Nath, V., Hansen, C., Parvathaneni, P., Blaber, J., Gao, Y., Neher, P., Aydogan, D.B., Shi, Y., Ocampo-Pineda, M., Schiavi, S., Daducci, A., Girard, G., Barakovic, M., Rafael-Patino, J., Romascano, D., Rensonnet, G., Pizzolato, M., Bates, A., Fischi, E., Thiran, J.P., Canales-Rodriguez, E.J., Huang, C., Zhu, H., Zhong, L., Cabeen, R., Toga, A.W., Rheault, F., Theaud, G., Houde, J.C., Sidhu, J., Chamberland, M., Westin, C.F., Dyrby, T.B., Verma, R., Rathi, Y., Irfanoglu, M.O., Thomas, C., Pierpaoli, C., Descoteaux, M., Anderson, A.W., Landman, B.A., 2019. Limits to anatomical accuracy of diffusion tractography using modern approaches. Neuroimage 185, 1–11.
Schumann, C.M., Amaral, D.G., 2005. Stereological estimation of the number of neurons in the human amygdaloid complex. J. Comparat. Neurol. 491, 320–329.
Sepehrband, F., Clark, K.A., Ullmann, J.F., Kurniawan, N.D., Leanage, G., Reutens, D.C., Yang, Z., 2015. Brain tissue compartment density estimated using diffusion-weighted MRI yields tissue parameters consistent with histology. Hum Brain Mapp. 36, 3687–3702.
Sepehrband, F., O'Brien, K., Barth, M., 2017. A time-efficient acquisition protocol for multipurpose diffusion-weighted microstructural imaging at 7 Tesla. Magn. Reson. Med. 78, 2170–2184.
Shah, A., Jhawar, S.S., Goel, A., 2012. Analysis of the anatomy of the Papez circuit and adjoining limbic system by fiber dissection techniques. J. Clin. Neurosci. 19, 289–298.
Smith, S.M., 2002. Fast robust automated brain extraction. Hum Brain Mapp. 17, 143–155.
Solano-Castiella, E., Anwander, A., Lohmann, G., Weiss, M., Docherty, C., Geyer, S., Reimer, E., Friederici, A.D., Turner, R., 2010. Diffusion tensor imaging segments the human amygdala *in vivo*. Neuroimage 49, 2958–2965.
Sorrells, S.F., Paredes, M.F., Velmeshev, D., Herranz-Pérez, V., Sandoval, K., Mayer, S., Chang, E.F., Insausti, R., Kriegstein, A.R., Rubenstein, J.L., Manuel Garcia-Verdugo, J., Huang, E.J., Alvarez-Buylla, A., 2019. Immature excitatory neurons develop during adolescence in the human amygdala. Nature Commun. 10, 2748.
Sowell, E.R., Trauner, D.A., Gamst, A., Jernigan, T.L., 2002. Development of cortical and subcortical brain structures in childhood and adolescence: a structural MRI study. Dev. Med. Child Neurol. 44, 4–16.
Spitzer, N.C., 2006. Electrical activity in early neuronal development. Nature 444, 707–712.
Tamnes, C.K., Herting, M.M., Goddings, A.L., Meuwese, R., Blakemore, S.J., Dahl, R.E., Guroglu, B., Raznahan, A., Sowell, E.R., Crone, E.A., Mills, K.L., 2017. Development of the cerebral cortex across adolescence: a multisample study of inter-related longitudinal changes in cortical volume, surface area, and thickness. J. Neurosci. 37, 3402–3412.
Tanner, J.M., 1981. Growth and maturation during adolescence. Nutr. Rev. 39, 43–55.
Thomas, C., Ye, F.Q., Irfanoglu, M.O., Modi, P., Saleem, K.S., Leopold, D.A., Pierpaoli, C., 2014. Anatomical accuracy of brain connections derived from diffusion MRI tractography is inherently limited. Proc. Natl. Acad. Sci. USA 111, 16574–16579.
Tustison, N.J., Avants, B.B., 2013. Explicit B-spline regularization in diffeomorphic image registration. Front Neuroinf. 7, 39.
Tyszka, J.M., Pauli, W.M., 2016. *In vivo* delineation of subdivisions of the human amygdaloid complex in a high-resolution group template. Hum Brain Mapp. 37, 3979–3998.
Von Der Heide, R.J., Skipper, L.M., Klobusicky, E., Olson, I.R., 2013. Dissecting the uncinate fasciculus: disorders, controversies and a hypothesis. Brain 136, 1692–1707.
Walhovd, K.B., Johansen-Berg, H., Karadottir, R.T., 2014. Unraveling the secrets of white matter–bridging the gap between cellular, animal and human imaging studies. Neuroscience 276, 2–13.
Wasserthal, J., Neher, P.F., Maier-Hein, K.H., 2018. Tract orientation mapping for bundle-specific tractography. In: Proceedings of the 21st International Conference on Medical Image Computing and Computer Assisted Intervention (MICCAI). Springer, Cham, Granada, Spain, pp. 36–44.
A SAS Program for the 2000 CDC Growth Charts (ages 0 to <20 years) 2019 Division of Nutrition, Physical Activity, and Obesity, National Center for Chronic Disease Pre-

vention and Health Promotion, Centers for Disease Control and Prevention Atlanta, GA.
Wechsler, D., 2011. Wechsler Abbreviated Scale of Intelligence (2nd ed. (WASI-II)), NCS Pearson, San Antonio, TX (2011).
Weller, K.L., Smith, D.A., 1982. Afferent connections to the bed nucleus of the stria terminalis. Brain Res 232, 255–270.
Yakovlev, P., Lecours, A., 1967. The myelogenetic cycles of regional maturation of the brain. A. Minkowski (Ed.), Regional Development of the Brain Early in Life, Blackwell Scientific Publications Inc., Boston, Massachusets (1967), pp. 3-70.
Yang, Y., Wang, J.Z., 2017. From structure to behavior in basolateral amygdala-hippocampus circuits. Front Neural Circuits 11, 86.
Yizhar, O., Klavir, O., 2018. Reciprocal amygdala-prefrontal interactions in learning. Curr. Opin. Neurobiol. 52, 149–155.
Zhang, H., Schneider, T., Wheeler-Kingshott, C.A., Alexander, D.C., 2012. NODDI: practical *in vivo* neurite orientation dispersion and density imaging of the human brain. Neuroimage 61, 1000–1016.
Zhang, H., Yushkevich, P.A., Alexander, D.C., Gee, J.C., 2006. Deformable registration of diffusion tensor MR images with explicit orientation optimization. Med. Image Anal. 10, 764–785.
Zhang, S., Peng, H., Dawe, R.J., Arfanakis, K., 2011. Enhanced ICBM diffusion tensor template of the human brain. Neuroimage 54, 974–984.